



Rate Effects on Shear Deformation of Rough Limestone Discontinuities

Doron Morad^{1,2} · Yossef H. Hatzor¹ · Amir Sagy²

Received: 26 August 2018 / Accepted: 5 December 2018
© Springer-Verlag GmbH Austria, part of Springer Nature 2019

Abstract

The relationship between slip velocity, resistance to shear, and geometrical evolution of initially rough limestone surfaces is investigated in servo-controlled direct shear experiments. We focus on shear stress evolution throughout the deformation process, as function of the shear rates applied. Direct shear tests are performed on tensional fractures positioned in a perfectly mating configuration, using a hydraulic, closed-loop, servo-controlled system. The discontinuities are sheared to prescribed displacement target of 10 mm under a constant normal stress of 5 MPa while shear stress and dilation are recorded under controlled shear rates between 0.1 and 50 μ /s. Surface geometry is measured using laser profilometer before and after tests, and roughness evolution is statistically quantified. We find that, before peak shear stress is attained, the shear stiffness increases with slip velocity, manifesting asperity strain hardening during this largely elastic deformation stage. Peak shear stress and stress drop, however, are both inversely proportional to velocity, indicating velocity weakening coupled with rate-dependent healing of the interfaces. The final roughness of the sheared surfaces increases moderately with increasing slip velocity indicating enhanced fragmentation and brittle deformation with increasing shear rate.

Keywords Rock discontinuities · Slip velocity · Multiscale roughness · Shear stiffness · Peak and residual shear strength

1 Introduction

Surface topography is a dominant factor controlling the frictional resistance offered by rock discontinuities. The first attempt to quantify the role of roughness in friction of rock joints was by Patton (1966) who conducted direct shear tests on surfaces with a constant roughness angle and, as a result, proposed a bi-linear failure criterion. His results showed that under low normal stress, shear resistance is controlled by both the pure friction of the smooth interface material and by the artificial roughness component, and that the contribution of the roughness component is diminished at higher normal stresses. Patton's work was complemented by the observations of Rangers (1970) on the relationship between sliding distance and roughness degradation. Ladanyi and Archambault (1970) proposed a theoretically based shear failure criterion that considers the initial roughness, asperity

contact area, and roughness degradation through shear. Barton (1976) has incorporated some of these original observations in his empirical shear strength criterion for rough rock discontinuities that also considers the strength of the asperity material and the degree of alteration of the surface. Ever since, the relationship between surface roughness and friction has intrigued numerous researchers in engineering rock mechanics (e.g., Cook 1992; Crawford and Curran 1981; Grasselli and Egger 2003; Liu et al. 2018; Seidel and Haberfield 2002; Zhao 1997).

While surface geometry is a principle factor in friction and contact mechanics (Bowden and Tabor 1950; Persson 2006) proven to influence the shear strength of discontinuities, friction laws in earthquake mechanics tended to ignore surface roughness based on experimental results which demonstrated that, under tectonic stresses, friction is almost independent of surface geometry (Byerlee 1978). Recent seismological, experimental, and theoretical studies, however, clearly demonstrate potential effects of roughness amplitude and spatial characteristics on slip dynamics, stress drop, and energy dissipation in natural faulting processes (e.g., Fang and Dunham 2013; Harbord et al. 2017; Tal et al. 2018; Wang and Bilek 2011; Zielke et al. 2017). In contrast to the conditions applied in many laboratory friction

✉ Amir Sagy
asagy@gsi.gov.il

¹ Department of Geological and Environmental Science, Ben Gurion University of the Negev, 84105 Beer Sheva, Israel

² Geological Survey of Israel, 30 Malkhe Israel, 95501 Jerusalem, Israel

experiments, natural fault topography is scale-dependent or self-affine along large spatial scales (Candela et al. 2012; Power et al. 1988). Moreover, natural slip surfaces are interlocked or partly cohesive and, therefore, cannot be treated using simple asperity models. Geological faulting processes, indeed, exhibit mixed multiscale failure modes associated with frictional slip failure coupled with fracture of intact rock during the entire slip event (Ohnaka 2003).

Strain rate is one of the basic parameters that control deformation and strength of geological materials, both intact rocks as well as rock discontinuities (e.g., Byerlee and Brace 1968; Heard 1963; Boneh and Reches 2017). The mechanical reaction of intact carbonate specimens under triaxial compression to increasing strain rates has typically been expressed by higher rigidity as well as more pronounced brittle failure (Rutter 1972). The frictional response of rock discontinuities to rate has been described by rate and state friction laws (e.g., Dieterich 1972, 1979; Marone 1998; Ruina 1983), with a particular emphasis on nucleation of dynamic slip. It has further been demonstrated that, when sliding velocity approaches earthquake slip rates, friction is drastically reduced (e.g., Di Toro et al. 2011; Reches and Lockner 2010; Tsutsumi and Shimamoto 1997).

While rate effect on post-peak steady-state friction has been studied extensively (e.g., Dieterich 1972, 1979; Marone 1998; Ruina 1983), a little attention has been given to the relationship between the rate of loading and the elastic response of the sliding surface before onset of plastic slip. This relationship is scaled by the “shear stiffness” relating between incremental shear stress and the corresponding shear displacement before peak shear stress is achieved (Goodman 1974, 1989). The influence of slip rate on shear stiffness in frictional systems has only recently began to be explored in engineering rock mechanics (e.g., Atapour and Moosavi 2014), although this effect must be very important when trying to assess, quantitatively, stress accumulation on rock discontinuities during creep episodes in deep-seated landslides, or across geological faults during inter-seismic periods.

Here, we test the influence of loading rate on shear deformation of interlocked, rough discontinuities by shearing Limestone surfaces of 10 cm length with roughness amplitudes of up to 1 cm to target displacement of 10 mm. In our experiments, we also aim to simulate some aspects of shear across natural faults, based on the assumption that natural fault surfaces consist of geometrical irregularities in a large range of scales, including those which are larger than the typical slip amount in a given slip event (Power et al. 1988; Brodsky et al. 2016), as is the case here. By continuous measurements of stresses and displacements in controlled direct shear experiments and by measuring surface roughness with a high-resolution laser profilometer before and after each test, we explore how shear stiffness, shear

strength, and roughness evolution are affected by slip rate and discuss applications to deformation and slip of natural discontinuities and tectonic faults.

2 Experimental Methods

To simulate shear deformation of multiscale rough interlocked surfaces, we first generate surfaces with statistically similar initial roughness characteristics, by fracturing prismatic isotropic limestone beams using the four-point bending methodology (Fig. 1a). The limestones used as starting material are from the Upper Cretaceous Judea Group (locally known as B’ina Formation) in central Israel. The limestone is characterized by dry density of 2565 (kg/m³), porosity of 5%, dynamic and static Young’s modulus of 69 and 57 GPa respectively, Poisson’s ratio of 0.28, and tensile strength (as obtained using the Brazilian method) of 5.7 MPa. The fresh surfaces of the tensile fractures are about 10 cm long by 8 cm wide, with multiscale roughness amplitudes reaching up to ~1 centimeter. We scan the topography of the surfaces with laser profilometer (Fig. 1b) enabling high-resolution topographical measurements (Fig. 1c). After scanning the initial roughness, the upper and lower blocks are placed in a shear box (Fig. 1e) in a perfectly mating configuration.

Direct shear tests are performed using a hydraulic, closed-loop, servo-controlled system which is comprised of a load frame with normal load capacity of 1000 kN and stiffness of 7.0 MN/m, and a shear system with shear load capacity of 300 kN and stiffness of 3.5 MN/m. During shear, the lower part of the shear system slides on frictionless rollers positioned between the shear system and the base platen of the load frame. The shear box dimensions are 200 mm × 200 mm × 300 mm high. The maximum specimen width and length are 150 mm × 150 mm with maximum height of 230 mm. The two interfaces are cast in the shear boxes in a completely mating configuration, so that, when initially loaded in the normal direction, the interlocked contact geometry is fully preserved.

All direct shear tests are performed under constant normal stress of 5 MPa and the tested interfaces are free to dilate or contract during shear. Vertical motion of the interfaces during shear is monitored using four LVDT transducers, each with 50 mm range and 0.25% linearity full scale, positioned on four corners of the shear box (see Fig. 1e).

The normal loading segment is performed under displacement control at a rate of 0.01 mm/s up to a target normal stress of 5 MPa. During the normal load segment, the outputs from the four vertical LVDT transducers are monitored and the normal stiffness of the tested surface is computed from the average vertical displacement. Once the normal stress target of 5 MPa is reached, the control

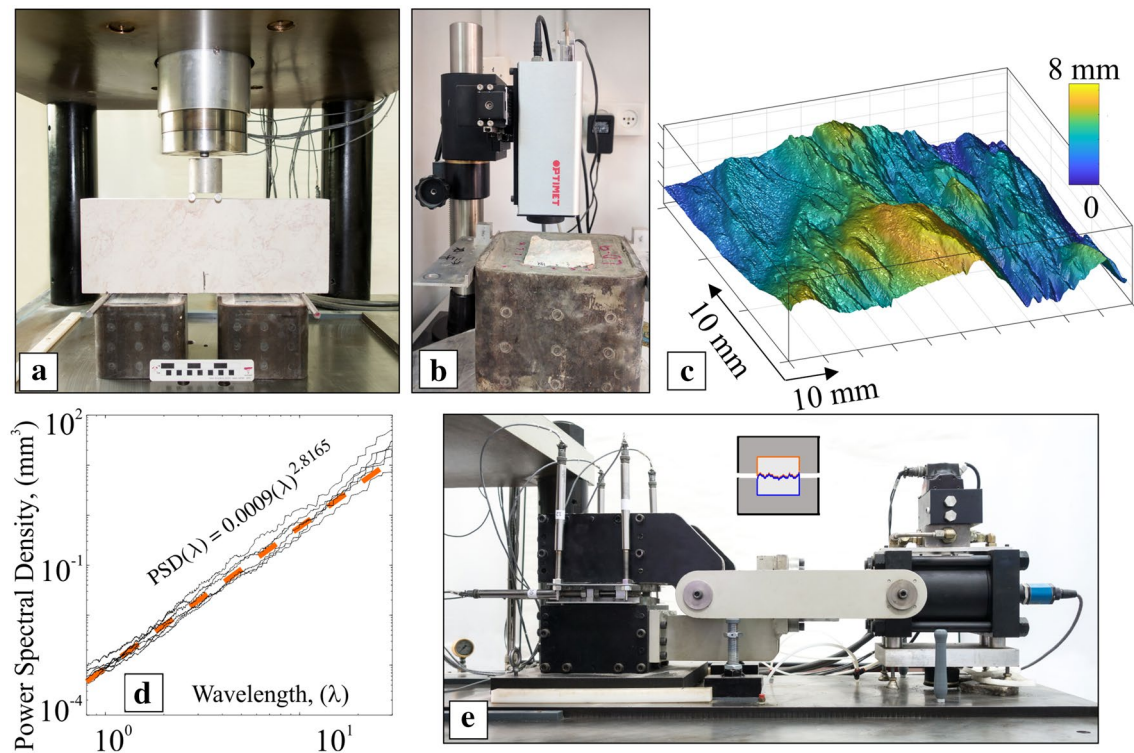


Fig. 1 Experimental methods. **a** Tensile splitting of a notched prismatic limestone beam by four-point bending to obtain similar initially rough surfaces. **b** Laser profilometer scanning of surfaces before and after shear. **c** 3D topographical imaging of the surface. **d** Initial power spectral density (PSD) values are presented as function of the

wavelength. Red dashed line represents average fitting to a power of 2.8, corresponding to a roughness exponent of 0.9. **e** The direct shear system showing the shear piston (right), shear box and displacement transducers, and normal load frame. Schematic illustration of the interlocked mating interface inside the shear box shown in inset

mode of the normal piston is switched to load control so as to maintain constant normal stress during the shear segments.

The shear segments are performed under displacement control at displacement rates between 0.1 and 50 $\mu\text{m/s}$ to a target displacement of 10 mm. The shear displacement control signal is the average output from two horizontal LVDT transducers, with the same range and resolution as the vertical transducers, which are positioned very close to the sheared interface (see Fig. 1e).

After the target shear displacement is achieved, the test is terminated, the normal load is removed, and the shear box is opened without shearing back to the original position. Special care is taken to preserve the sheared surfaces which are cleaned from wear material and are scanned again.

The sheared surfaces are scanned after the tests to enable the roughness evolution analysis. To measure surface topography, we utilize the Optimet ConoScan 2000 system, consisting of three lenses for different resolution options, with 25 mm, 50 mm, and 75 mm focal distances. The sampling frequency in the direction of scanning can be adjusted to 1 μm steps, but, usually, is fixed at 100 μm . A single scan includes 640 parallel profiles that covers,

under the 75 mm lens, a width of 18.636 mm perpendicular to the scanning direction.

Surface roughness is commonly analyzed using the RMS values. RMS is the statistical standard deviation related to a mean reference, described in Eq. 1 for one vector (2D) as follows:

$$\text{RMS} = \left[\frac{1}{L} \int_0^L Y^2(x) dx \right]^{0.5}, \quad (1)$$

where L is the profile length, Y is the amplitude or height of a given point, and x is the distance along the profile. The RMS values of the entire surface are obtained from the average RMS values of all profiles for any measured length (Sagy et al. 2007), where higher RMS values correspond to rougher surface topography.

Roughness values parallel to the slip direction are also calculated in terms of power spectral density (PSD). Discrete Fourier Transform is obtained for each de-trended profile. For every given wavelength λ , the PSD value is averaged from the values calculated from a few hundred profiles using Thomson (1982) method.

Fracture surface geometry that is invariant with length scale obeys the transformation:

$$\Delta x \rightarrow \lambda \Delta x \quad \Delta y \rightarrow \lambda^H \Delta y, \quad (2)$$

where Δx is the spacing in a given direction along the surface and Δy is the average height. The PSD of such surfaces may be described by a scaling law of the type:

$$\text{PSD}_{(\lambda)} = C\lambda^\beta, \quad (3)$$

where C and β are constants. In the special case of self-affine roughness, the β values are in the range of 1–3 and the RMS can be obtained from the PSD values as follows (Brown and Scholz 1985; Sagy et al. 2007):

$$\text{RMS} = \left[C / (\beta - 1) \right]^{0.5} L^{(\beta - 1)/2}, \quad (4)$$

where $K = \left[C / (\beta - 1) \right]^{0.5}$ and the roughness exponent $\xi = (\beta - 1)/2$.

3 Results

3.1 Mechanical Observations

Results of all direct shear tests are listed in Table 1 and plotted in Fig. 2a in shear stress vs. shear displacement space. The dilation as function of shear displacement is shown in Fig. 2b where contraction is positive. Similar values of normal stiffness are obtained for all the tests (see Table 1), indicating initially homogeneous elasticity and strength of the tested interfaces.

As the intimate interlocked contacts between the asperities are maintained during the normal loading segment, once the shear segment begins the initial response of the asperity material is assumed to be predominantly elastic. The shear stiffness is calculated accordingly for the initial displacement interval between 0 and 0.2 mm, before ultimate shear resistance is reached in any of the tested interfaces (inset in Fig. 2a), using linear regression. The shear stiffness values

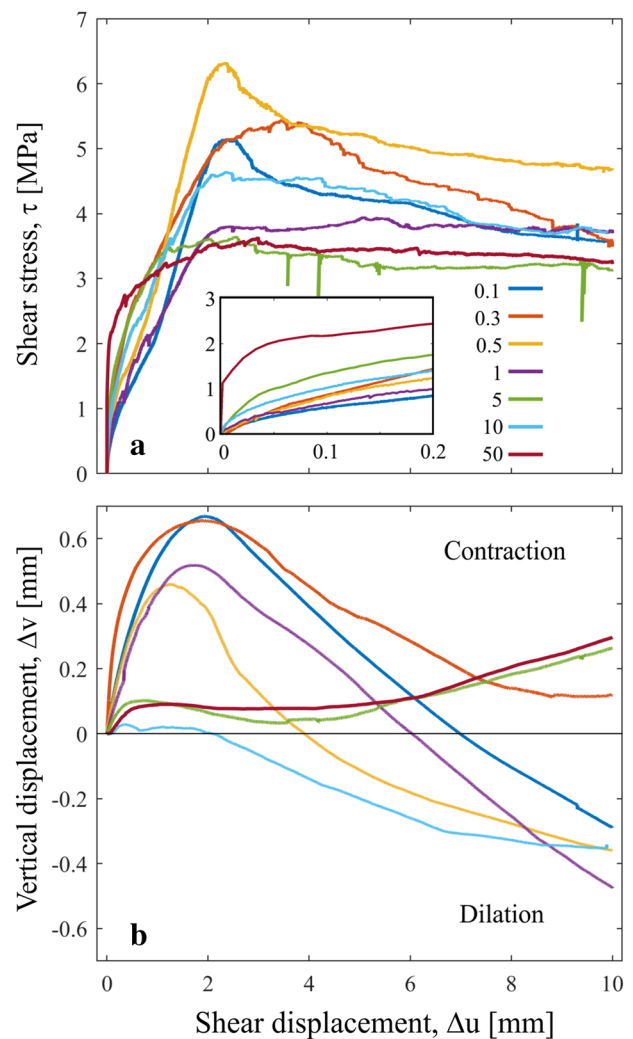


Fig. 2 Stress and vertical displacement evolution during direct shear experiments of rough interlocked slip surfaces. **a** Shear stress vs. shear displacement for all experiments with indicated rates in $\mu\text{m/s}$ (colors), the initial stage is enlarged in inset. All tests are performed under constant normal stress of 5 MPa. **b** Average vertical displacement through shear, obtained from the outputs of four vertical LVDT transducers (dilation is negative). (Color figure online)

Table 1 Results of direct shear tests

Specimen ID	Sliding velocity ($\mu\text{m/s}$)	Normal stiffness (MPa/mm)	Shear stiffness (MPa/mm)	Max contraction (mm)	Peak friction ($\tau_{\text{peak}}/\sigma_n$)	Residual friction (τ_r/σ_n)
LD-9	0.1	9.4	4.9	0.6691	1.0313	0.7090
LD-10	0.3	5.5	7.9	0.6551	1.0906	0.6983
LD-6	0.5	5.1	7.1	0.4601	1.2663	0.9380
LD-5	1	6.5	5.8	0.5187	0.7908	0.7398
LD-1	5	5.9	10.7	0.1019	0.7296	0.6270
LD-8	10	8.0	8.4	0.0284	0.9302	0.7414
LN-1	50	5.7	16.8	0.0904	0.7243	0.6449

obtained for the different tests (Table 1) manifest the influence of rate on shear stiffness. During this initial loading stage, the samples typically contract, and only begin to dilate when the shear stress approaches it to a maximum value (see Fig. 2b).

Mechanical properties as function of slip velocity are presented in Fig. 3. The shear stiffness exhibits strong rate dependence (Fig. 3a), increasing with increasing velocity. Peak friction coefficient, however, is inversely proportional to rate (Fig. 3b). Strain rate hardening, therefore, characterizes the largely elastic pre-peak stage, whereas peak friction exhibits a velocity weakening behavior. Post-peak sliding commences at residual friction coefficients between 0.7 and 0.8, with a much weaker correlation to velocity (open circles in Fig. 3b). Interestingly, “steady-state” sliding after 10 mm of displacement is only achieved in the three relatively fast rates (1, 5, 50 $\mu\text{m/s}$). Consequently, the characteristic D_c length (Scholz 1998; Ohnaka 2003) cannot be obtained for the slower experiments, as steady-state friction is not achieved in these experiments after 10 mm of displacement.

The transition from peak to post-peak sliding is rate-dependent, as well (Fig. 3c). The samples tested at the lower rates (0.1, 0.3, and 0.5 $\mu\text{m/s}$) all exhibit a distinct peak stress followed by a pronounced stress drop to post-peak sliding. Samples tested at the relatively faster rates (1, 5, 10, and 50 $\mu\text{m/s}$) do not exhibit a distinct peak stress and a smoother transition to post-peak sliding is observed.

Finally, the total amount of vertical contraction of the tested interfaces at peak friction is inversely related to velocity, with a very high correlation (Fig. 3d). We explain this

as another manifestation of velocity hardening at pre-peak, inferred above from the strong rate dependence of the shear stiffness (Fig. 3a). If, indeed, the interfaces respond more rigidly under increased velocity at the pre-peak stage, then they should also undergo less vertical contraction with increasing velocity.

Interestingly, the pre-peak stage of the relatively fast rates is characterized by local stress drop episodes, suggesting that small brittle events occur before peak friction is attained (Fig. 4).

3.2 Roughness Analysis

Visual inspection of the sheared interfaces after the tests reveals that, while parts are covered with grainy gouge material, the other parts exhibit penetrative fractures, with the remaining areas apparently undamaged. This observation implies that, even though shear displacement began at a perfectly matting configuration, in fact, only small parts of the surfaces remained in contact during slip.

We study the surface evolution using quantitative roughness analysis as described in the “Experimental Methods” section. Roughness is calculated by determining the RMS (Fig. 1d) and the power spectral density (PSD) of the profiles, the latter of which provides the mean amplitude in a given wavelength (Nayak 1971). Based on hundreds of profiles measured parallel to the slip direction, our data demonstrate that the PSD values before and after slip can be described well by a power law in the range of the measured scales, with roughness exponent (ξ) values of 1–0.8. These

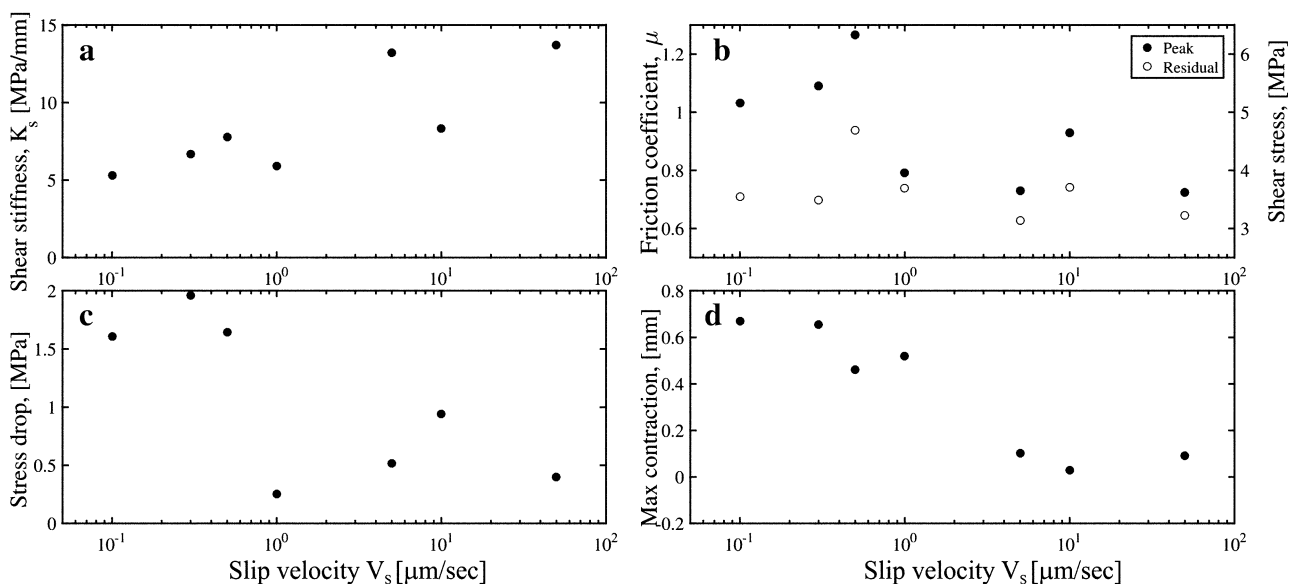
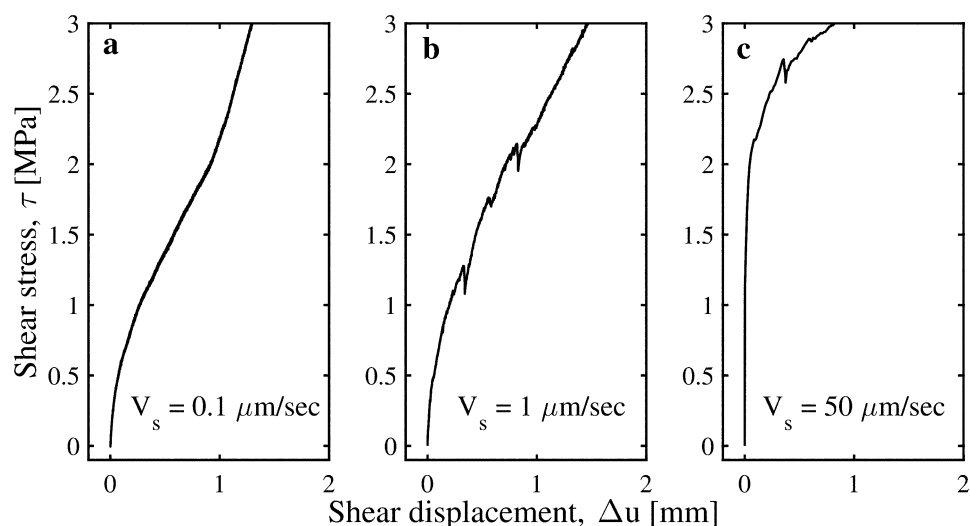


Fig. 3 Rate dependence of shear deformation. **a** Shear stiffness exhibits strain rate hardening (see text). **b** Peak and residual (after 10 mm of displacement) friction and corresponding shear stress values. **c**

Calculated stress drop (difference between peak and residual shear stress) and **d** maximum contraction of the interface at peak shear stress

Fig. 4 Shear stress evolution during initial segment of direct shear tests, for shear rates of 0.1 $\mu\text{m/s}$ (a), 1 $\mu\text{m/s}$ (b), and 50 $\mu\text{m/s}$ (c). While the curve in a is smooth, small stress drop events appear in b and c. The increase of shear stiffness as function of slip velocity can be appreciated from the steep initial part of the curve in c



values are similar to values obtained in our lab (Badt et al. 2016; Davidesko et al. 2014) in the previous studies using the same starting material and preparation method. In most of our experiments, roughness values for any given wavelength increase after slip (Fig. 5a, b).

To test the influence of slip velocity on the final roughness profile, we compare the PSD of the different experiments before and after shear. Because the initial roughness profiles in the different samples are similar but not identical, we first normalize the roughness differences by dividing the pre-shear by the post-shear roughness vectors, [final PSD(λ)/initial PSD(λ)] for any given run (Davidesko et al. 2014), the results of our tests are shown in Fig. 5c. We find that the roughness profiles evolve more strongly

with increasing slip velocity. Under the slow slip velocities of 0.1 (see Fig. 5b) and 0.3 $\mu\text{m/s}$ the PSD ratio approaches 1.0 for most wavelengths, indicating less brittle damage of the sheared interfaces (Badt et al. 2016). However, at the higher slip velocities of 5 and 10 $\mu\text{m/s}$, the PSD ratio increases and approaches 2.0 for most wavelengths, indicating increased brittleness of the sheared interfaces with increasing velocity. We find that the scale of the troughs at the sheared interfaces corresponds to the size of the asperities comprising the roughness profile (Fig. 6) indicating that the velocity-enhanced brittle deformation is concentrated at the asperities that are in contact in the pre-peak stage, and are plucked out at the post-peak stage, leaving behind a rougher interface.

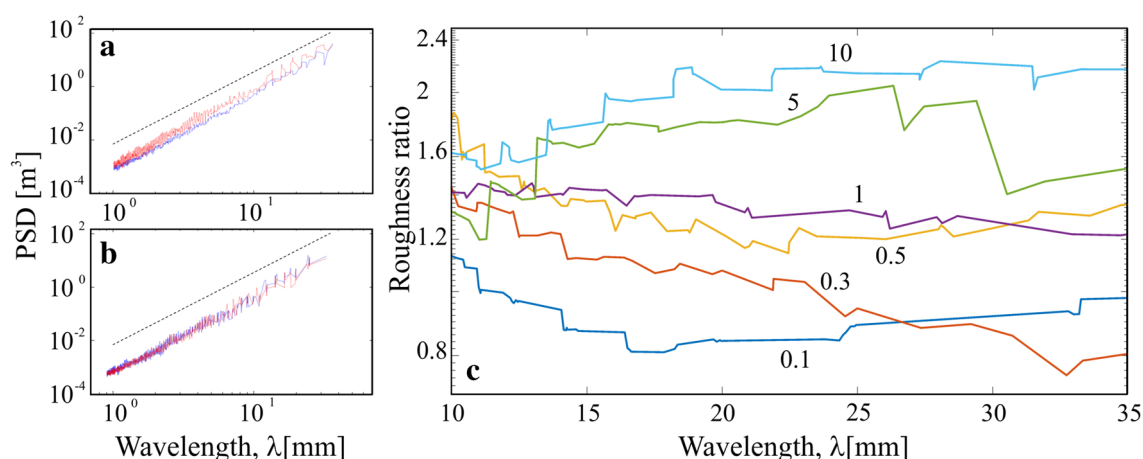


Fig. 5 Evolution of surface roughness as a function of shear rate parallel to the slip direction. Power spectral density values are presented as function of the wavelength for shear rate of 10 $\mu\text{m/s}$ (a) and 0.1 $\mu\text{m/s}$ (b). Measurements are averaging thousands of profiles from the two mated surfaces. Note moderate roughening of the final sur-

faces (red line) comparing to the initial surfaces (blue line). Dotted line represents roughness exponent of 0.9. c Roughness ratio [final PSD(λ)/initial PSD(λ)] for six samples showing moderate increase of this ratio with increasing shear rate in the largest measuring scales. Color code as in Fig. 2a. (Color figure online)

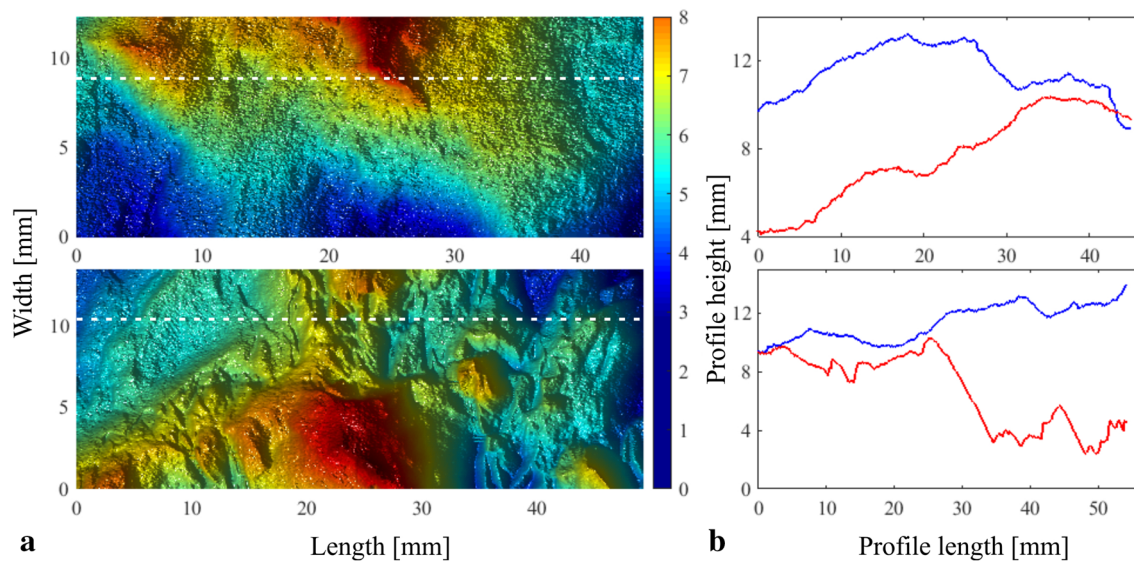


Fig. 6 **a** Surface topography of two samples sheared under rates of $0.1 \mu\text{m/s}$ (upper panel) and $10 \mu\text{m/s}$ (bottom panel). Colors represent height in millimeters. Slip direction is horizontal. **b** Examples for

two profiles (dashed lines in **a**) before (blue line) and after (red line) shearing. (Color figure online)

Finally, to complete a geo-tribology analysis, the wear material produced during shear is measured. The vast majority of the wear volume is characterized by brittle and relatively large fractured fragments. We calculate the volume of the wear material by subtracting the initial topography level from the final one (see Badt et al. 2016). In general, we do not find a robust correlation between slip velocities and wear rate. We further discuss this issue in Sect. 4.

4 Discussion

We have shown that both pre- and post-peak shear deformation of multiscale interlocked rough surfaces is slip-rate-dependent. The pre-peak deformation stage exhibits strain hardening behavior as indicated by positive correlation between shear stiffness and slip velocity (Fig. 3a), and negative correlation between maximum contraction at peak friction and slip velocity (Fig. 3d). Peak friction is inversely proportional to slip velocity (solid circles in Fig. 3b), suggesting that velocity weakening begins even before ultimate shear strength is reached. Although the velocity weakening is also observed at post-peak, the correlation with rate is much weaker (open symbols in Fig. 3b). These two rate-dependent processes are considered by the first-order rate effects due to the strong statistical correlation that we obtained between them and the imposed shear rate. We note that some deviations do exist in our results, for example, in the $10 \mu\text{m/s}$ rate experiment, probably because the initial roughness is similar but not identical between our tested interfaces (Fig. 1d).

While interlocking in our experiments is almost perfect initially, only portions of the contacts deform inelastically, most likely due to the heterogeneous stress concentrations across the rough surfaces. We associate the initial contraction observed in Fig. 2b before peak shear stress is reached with this interlocking deformation. The onset of dilatation indicates transition from contact crushing to sliding on the surviving asperities, as also observed in direct shear tests that do not necessarily ensure good initial interlocking (e.g., Sagy et al. 2017). This behavior has also been observed under higher normal stresses although with smaller contraction and with much more contact area being formed (See Badt et al. 2016). We conclude, therefore, that the primary influence of interlocking is on the stress and displacement evolution before peak shear stress is reached, during which both fracturing and sliding take place.

We also observe two second-order rate effects. First, the transition from peak to post-peak sliding is found to be rate-dependent, with a smoother transition observed at the faster rates and a more pronounced stress drop observed at the slower rates (Figs. 2a, 3c), possibly a manifestation of rate-dependent healing processes. Episodic “fore-shock” events preceding peak friction are detected in the faster velocity tests (Fig. 4), possibly manifesting rate-dependent brittle deformation at the pre-peak stage. Second, the damage evolution of the sheared interfaces is found to be rate-dependent, as well, expressed by increased roughness amplitude following shear, the scale of which corresponds to the scale of the initial asperities (Fig. 5).

This pattern of damage evolution might explain the weak correlation between slip velocity and wear accumulation.

We suggest that two competing factors come into play here. In the faster shear velocities, strain hardening at the pre-peak region may cause brittle deformation of the asperity materials, thus, increasing wear accumulation. In the slow rate tests, on the other hand, more stress is being built up on the asperities before peak stress is attained, and this could lead to crushing failure of the asperities once peak stress is attained, resulting, again, in increased wear production. It should be pointed out that a negative correlation between slip velocity and wear accumulation rate has been observed in rotary shear experiments (Boneh et al. 2013, 2017), yet these experiments were conducted at steady-state conditions and, therefore, were much less influenced by the initial roughness.

The positive correlation that we obtain between shear stiffness and slip velocity (Fig. 3a) suggests that elastic deformation governs the pre-peak loading stage, primarily between 0 and 0.2 mm of shear displacement. This is supported by the observed contraction of the asperities at this stage (Figs. 2b, 3d), a process that could be analogous to volume decrease during the elastic deformation of intact rocks under compression. During compression of brittle rocks, the stiffness, as scaled by the Young's modulus, typically increases with increasing strain rate (e.g., Lajtai et al. 1991). However, whereas, in compression, ultimate compressive strength is proportional to strain rate (e.g., Heard 1963); here, we find that, in direct shear, ultimate shear strength is inversely proportional to rate. Indeed, velocity weakening of peak friction during direct shear of rough surfaces has been observed before (e.g., Biran et al. 2009; Crawford and Curran 1981). We, therefore, suggest that velocity weakening processes begin before ultimate shear strength is actually reached.

We have shown that shear resistance is influenced by brittle deformation mechanisms distributed at varying degrees across the different loading stages. At the pre-peak stage stress localization at the contacting asperities controls the brittle deformation, as has also been observed by Boneh and Reches (2018). The brittle plucking of asperities and the roughening of the surface observed at the post-peak sliding phase demonstrate rate induced rigidity that possibly carries over from the pre-peak to the post-peak deformation stage. At the post-peak stage, samples sliding at high slip velocities (1, 5, 50 $\mu\text{m/s}$) reach quasi-steady-state friction coefficient of ~ 0.7 , a value that has been observed for slip on gouge zones in sheared limestone interfaces (Tesei et al. 2017), and is typical for rock discontinuities in general (Byerlee 1978). The increasing brittle deformation in the relatively fast runs appears to enhance gouge generation and friction degradation. We note significant variations of roughness as a function of slip velocity (Fig. 5), at least for the rates used in our experiments. These variations, however, are less pronounced than the variations observed as function of normal stress

(Badt et al. 2016) and amount of displacement (Davidesko et al. 2014).

We conclude that multiscale geometrical irregularities across natural discontinuity surfaces such as joints and faults impose a hybrid nature of deformation consisting of coupled fracture and friction (Ohnaka 2003). We propose that both the initial surface roughness as well as the rate of displacement along the entire cycle of loading and deformation, as observed here, are significant for faulting mechanics.

Finally, although the direct applications of our experiments are for the low normal stress regime, we suggest that some of the observations presented here might be relevant to tectonic faulting and earthquakes. While peak friction of rock surfaces at seismogenic depths is mainly a function of normal stress (Byerlee 1978), interlocking conditions imply that stress patterns, internal failure initiation, location, and magnitude along rough faults strongly depend on fault geometry (Saucier et al. 1992; Chester and Chester 2000). In addition, slip velocity strongly influences stress evolution and, as a result, might affect the deformation patterns of the surface as well as off fault damage. In this sense, our experiments might model a section in a large rough fault loaded during an inter-seismic period. According to our observations, slower displacement velocities facilitate healing that causes strengthening; therefore, more elastic strain energy can be absorbed in the system before local peak stress is achieved. When this section finally yields, it is usually associated with a larger stress drop (Fig. 3c). We speculate that the observed positive correlation between plate motion rate and number of earthquakes (Ide 2013) and between convergence rates and the value of the Gutenberg Richter b value (Nishikawa and Ide 2014) found in subduction zones might reflect similar processes as presented and discussed in this paper.

5 Conclusions

Rough surfaces are sheared at different displacement rates under constant normal stress. We find that resistance to shear, during both pre- and post-peak deformation, is rate-dependent, and we demonstrate that shear deformation of rough interlocked surfaces consists of unique characteristics that are different from shear deformation of intact rock material as well as smooth pre-existing discontinuities:

- Surface roughness increases with slip velocity suggesting rate-dependent brittle deformation carries over to the post-peak regime.
- While shear stiffness increases with rate, peak friction actually decreases with rate.
- Fore-shock like events preceding peak stress are observed in the high rate experiments, suggesting strain rate hard-

ening and increasing brittle deformation in the our higher slip velocity tests.

- Stress drop is enhanced in the slow rate experiments, indicating that rate-dependent healing processes ensue before transition to post-peak deformation.

We believe that our tests simulate important aspects of slip deformation across geological faults, based on the assumption that they are characterized by multiscale geometrical amplitudes including those which are equal to or larger than the typical slip amount in a given slip event. We demonstrate the significance of the initial roughness and shear rate to faulting mechanics from nucleation to slip of a segment, with a particular emphasis on natural carbonate discontinuities and tectonic faults at shallow crustal zones.

Acknowledgements This research is funded by Israel Science Foundation through contract no. ISF 937/17. We thank Ze'ev Reches and another anonymous reviewer for reviewing an earlier version of this manuscript and for their helpful comments.

References

- Atapour H, Moosavi M (2014) The influence of shearing velocity on shear behavior of artificial joints. *Rock Mech Rock Eng* 47:1745–1761
- Badt N, Hatzor YH, Toussaint R, Sagy A (2016) Geometrical evolution of interlocked rough slip surfaces: the role of normal stress. *Earth Planet Sc Lett* 443:153–161
- Barton N (1976) The shear strength of rock and rock joints. *Int J Rock Mech Min* 13:255–279
- Biran O, Hatzor YH, Ziv A (2009) Micro-scale roughness effects on the friction coefficient of granite surfaces under varying levels of normal stress. In: Hatzor Y, Sulem J, Vardoulakis I (eds) *Shear physics at the meso-scale in earthquake and landslide mechanics*. CRC Press, Boca Raton, pp. 145–158
- Boneh Y, Reches ZE (2017) Geotribology-Friction, wear, and lubrication of faults. *Tectonophysics*
- Boneh Y, Sagy A, Reches Z (2013) Frictional strength and wear-rate of carbonate faults during high-velocity, steady-state sliding. *Earth Planet Sci Lett* 381:127–137
- Bowden F, Tabor D (1950) *The friction and lubrication of solids*. Oxford University Press, Oxford
- Brodsky EE, Kirkpatrick JD, Candela T (2016) Constraints from fault roughness on the scale-dependent strength of rocks. *Geology* 44:19–22
- Brown SR, Scholz CH (1985) Broad bandwidth study of the topography of natural rock surfaces. *J Geophys Res* 90:512,575–512,582
- Byerlee J (1978) Friction of rocks. *Pure appl Geophys* 116:615–626
- Byerlee JD, Brace WF (1968) Stick slip, stable sliding, and earthquakes—effect of rock type, pressure, strain rate, and stiffness. *J Geophys Res* 73:6031–6037
- Candela T, Renard F, Klinger Y, Mair K, Schmittbuhl J, Brodsky EE (2012) Roughness of fault surfaces over nine decades of length scales. *J Geophys Res-Solid Earth* 117
- Chester FM, Chester JS (2000) Stress and deformation along wavy frictional faults. *J Geophys Res: Solid Earth* 105(B10):23421–23430
- Cook NGW (1992) Natural joints in rock—mechanical, hydraulic and seismic behavior and properties under normal stress. *Int J Rock Mech Min Sci Geomech Abstracts* 29:198–223
- Crawford AM, Curran JH (1981) The influence of shear velocity on the frictional resistance of rock discontinuities. *Int J Rock Mech Min* 18:505–515
- Davidesko G, Sagy A, Hatzor YH (2014) Evolution of slip surface roughness through shear. *Geophys Res Lett* 41:1492–1498
- Di Toro G, Han R, Hirose T, De Paola N, Nielsen S, Mizoguchi K, Ferri F, Cocco M, Shimamoto T (2011) Fault lubrication during earthquakes. *Nature* 471:494–494+
- Dieterich JH (1972) Time-dependent friction in rocks. *J Geophys Res* 77:3690–3697
- Dieterich JH (1979) Modeling of rock friction, 1: Experimental results and constitutive equations. *J Geophys Res* 84:2161–2168
- Fang ZJ, Dunham EM (2013) Additional shear resistance from fault roughness and stress levels on geometrically complex faults. *J Geophys Res-Sol Ea* 118:3642–3654
- Goodman RE (1974) The mechanical properties of joints. In: *Proc. 3rd Conference ISRM, Denver CO*, pp. 127–140
- Goodman RE (1989) *Introduction to rock mechanics*, 2nd edn. Wiley, New York
- Grasselli G, Egger P (2003) Constitutive law for the shear strength of rock joints based on three-dimensional surface parameters. *Int J Rock Mech Min* 40:25–40
- Harbord CWA, Nielsen SB, De Paola N, Holdsworth RE (2017) Earthquake nucleation on rough faults. *Geology* 45:931–934
- Heard HC (1963) Effect of large changes in strain rate in the experimental deformation of Yule marble. *J Geol* 71:162
- Ide S (2013) The proportionality between relative plate velocity and seismicity in subduction zones. *Nat Geosci* 6(9):780
- Ladanyi B, Archambault G (1970) Simulation of shear behaviour of a jointed rock mass. In: *Proc. 11th Symposium on Rock Mechanics*. AIME, New York, pp. 105–125
- Lajtai EZ, Duncan EJS, Carter BJ (1991) The effect of strain rate on rock strength. *Rock Mech Rock Eng* 24:99–109
- Liu QS, Tian YC, Ji PQ, Ma H (2018) Experimental investigation of the peak shear strength criterion based on three-dimensional surface description. *Rock Mech Rock Eng* 51:1005–1025
- Marone C (1998) The effect of loading rate on static friction and the rate of fault healing during the earthquake cycle. *Nature* 391:69–72
- Muhuri SK, Dewers TA, Scott Jr TE, Reches ZE (2003) Interseismic fault strengthening and earthquake-slip instability: Friction or cohesion? *Geology* 31(10):881–884
- Nayak PR (1971) Random process model of rough surfaces. *J Lubr Technol* 93:398
- Nishikawa T, Ide S (2014) Earthquake size distribution in subduction zones linked to slab buoyancy. *Nat Geosci* 7(12):904
- Ohnaka M (2003) A constitutive scaling law and a unified comprehension for frictional slip failure, shear fracture of intact rock, and earthquake rupture. *J Geophys Res-Solid Earth* 108
- Patton FD (1966) Multiple modes of shear failure in rock. In: *Proc. 1st Congr. Int. Soc. Rock Mech. ISRM, Lisbon*, pp. 509–513
- Persson BNJ (2006) Contact mechanics for randomly rough surfaces. *Surf Sci Rep* 61:201–227
- Power WL, Tullis TE, Weeks JD (1988) Roughness and wear during brittle faulting. *J Geophys Res-Solid Earth Planets* 93:15268–15278
- Rangers N (1970) Influence of surface roughness on friction properties of rock planes. In: *Proc. 2nd Cong. ISRM, Bergamo*, pp. 229–234
- Reches Z, Lockner DA (2010) Fault weakening and earthquake instability by powder lubrication. *Nature* 467:452–102
- Ruina A (1983) Slip instability and state variable friction laws. *J Geophys Res* 88:310,359–310,370
- Rutter EH (1972) Effects of strain-rate changes on strength and ductility of solenhofen limestone at low temperatures and confining pressures. *Int J Rock Mech Min Sci* 9:183–189

- Sagy A, Brodsky EE, Axen GJ (2007) Evolution of fault-surface roughness with slip. *Geology* 35:283–286
- Saucier F, Humphreys E, Weldon R (1992) Stress near geometrically complex strike-slip faults: application to the San Andreas fault at Cajon Pass, southern California. *J Geophys Res: Solid Earth* 97(B4):5081–5094
- Scholz CH (1998) Earthquakes and friction laws. *Nature* 391(6662):37
- Seidel JP, Haberfield CM (2002) A theoretical model for rock joints subjected to constant normal stiffness direct shear. *Int J Rock Mech Min* 39:539–553
- Tal Y, Hager BH, Ampuero JP (2018) The effects of fault roughness on the earthquake nucleation process. *J Geophys Res-Solid Earth* 123:437–456
- Tesei T, Carpenter BM, Giorgetti C, Scuderi MM, Sagy A, Scarlato P, Collettini C (2017) Friction and scale-dependent deformation processes of large experimental carbonate faults. *J Struct Geol* 100:12–23
- Thomson DJ (1982) Spectrum estimation and harmonic-analysis. *Proc IEEE* 70:1055–1096
- Tsutsumi A, Shimamoto T (1997) High-velocity frictional properties of gabbro. *Geophys Res Lett* 24:699–702
- Wang KL, Bilek SL (2011) Do subducting seamounts generate or stop large earthquakes? *Geology* 39, 819–822
- Zhao J (1997) Joint surface matching and shear strength. *JRC-JMC shear strength criterion. Int J Rock Mech Min Sci* 34:179–185
- Zielke O, Galis M, Mai PM (2017) Fault roughness and strength heterogeneity control earthquake size and stress drop. *Geophys Res Lett* 44:777–783

Publisher's Note Springer Nature remains neutral with regard to jurisdictional claims in published maps and institutional affiliations.